Supplementary Information

Regional Variations of Mercury's Crustal Density and Porosity from MESSENGER Gravity Data

Antonio Genova[1], Sander Goossens[2], Edoardo Del Vecchio[1], Flavio Petricca[1], Mikael Beuthe[3], Mark Wieczorek[4], Gianluca Chiarolanza[5,6], Gaetano di Achille[7], Giuseppe Mitri[5,6], Ivan di Stefano[1], Bernard Charlier[8], Erwan Mazarico[2], Peter James[9]

[1] Department of Mechanical and Aerospace Engineering, Sapienza University of Rome, Rome, 00184, Italy
[2] NASA Goddard Space Flight Center, Greenbelt, MD, USA.
[3] Royal Observatory of Belgium, Brussels, Belgium
[4] Université Côte d'Azur, Observatoire de la Côte d'Azur, CNRS, Laboratoire Lagrange, France
[5] Università d'Annunzio, Pescara, Italy
[6] International Research School of Planetary Sciences, Pescara, Italy
[7] INAF – Osservatorio Astronomico d'Abruzzo, Teramo, Italy
[8] Department of Geology, University of Liège, Sart Tilman, Belgium
[9] Department of Geosciences, Baylor University, Waco, TX 76798

Contents

Table S1 Lower and upper limits, and step size of the parameter of interest adjusted by using the model by *Broquet and Wieczorek* [1].

Parameter	Lower Bound	Upper Bound	Step Size
Crustal density $\boldsymbol{\rho_c}$ (kg m^{-3})	2200	3200	50
Load density $\boldsymbol{\rho_l}$ (kg m^{-3})	2200	3200	50
Loading parameter $\boldsymbol{L}$	-1	1	0.2
Crustal thickness $\boldsymbol{T_c}$ (km)	0	150	10
Elastic thickness $\boldsymbol{T_e}$ (km)	0	150	10

Table S2 Estimated parameters in the five locations of the local admittance analyses obtained by using top/bottom loading [1] and top loading model [2] to generate the synthetic gravity field. We report the estimates that are retrieved from a probability density distribution similar to Gaussian. Parameters that are undermined are classified as *U* or *B* that stand for uniform or bimodal probability density distribution, respectively.

Spherical	**Top Loading**			**Top/Bottom Loading**				
Cap Center	$\boldsymbol{\rho_c}$ (kg m^{-3})	$\boldsymbol{T_c}$ (km)	$\boldsymbol{T_e}$ (km)	$\boldsymbol{\rho_c}$ (kg m^{-3})	$\boldsymbol{\rho_l}$ (kg m^{-3})	$\boldsymbol{L}$	$\boldsymbol{T_c}$ (km)	$\boldsymbol{T_e}$ (km)
44ºN-286ºE	2597 ± 67	*U*	29 ± 6	*U*	2670 ± 160	-0.08 ± 0.12	51 ± 37	32 ± 6
53ºN-4ºE	2595 ± 33	*U*	*U*	*U*	2558 ± 88	0.06 ± 0.14	*U*	102 ± 35
70ºN-303ºE	2510 ± 52	*U*	27 ± 18	*U*	2455 ± 223	-0.17 ± 0.43	*U*	46 ± 38
72ºN-250ºE	2487 ± 39	*U*	*U*	*U*	2542 ± 125	-0.26 ± 0.31	*U*	*U*
38ºN-110ºE	*U*	60 ± 13	5 ± 4	*U*	2490 ± 252	-0.56 ± 0.25	91 ± 22	*B*

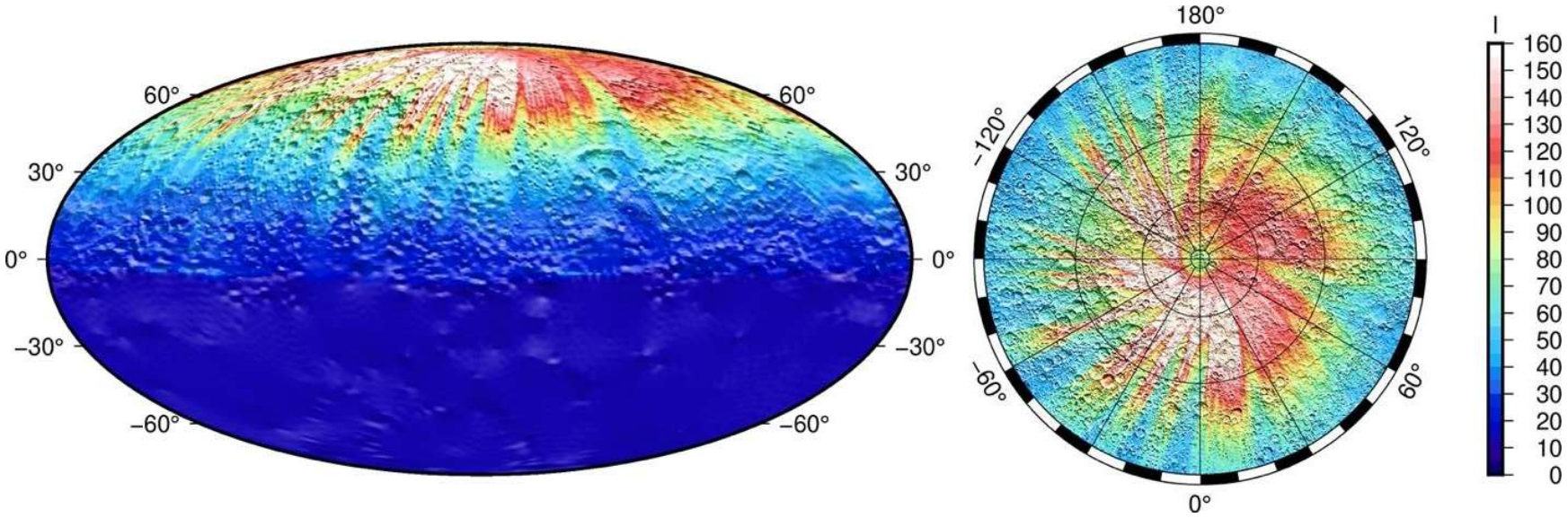

Figure S1 Degree strength map (**left**) in a Mollweide projection centered on 0° longitude and (**right**) in a polar stereographic projection from 30°N-latitude. This map was retrieved by comparing the expected acceleration profiles based on the Kaula power rule $C_l = \frac{10\times10^{-5}}{l^2}$ (see Eq. 2) and the formal errors of the covariance matrix of our unconstrained gravity solution (see Eq. 1 in the paper by [3]).

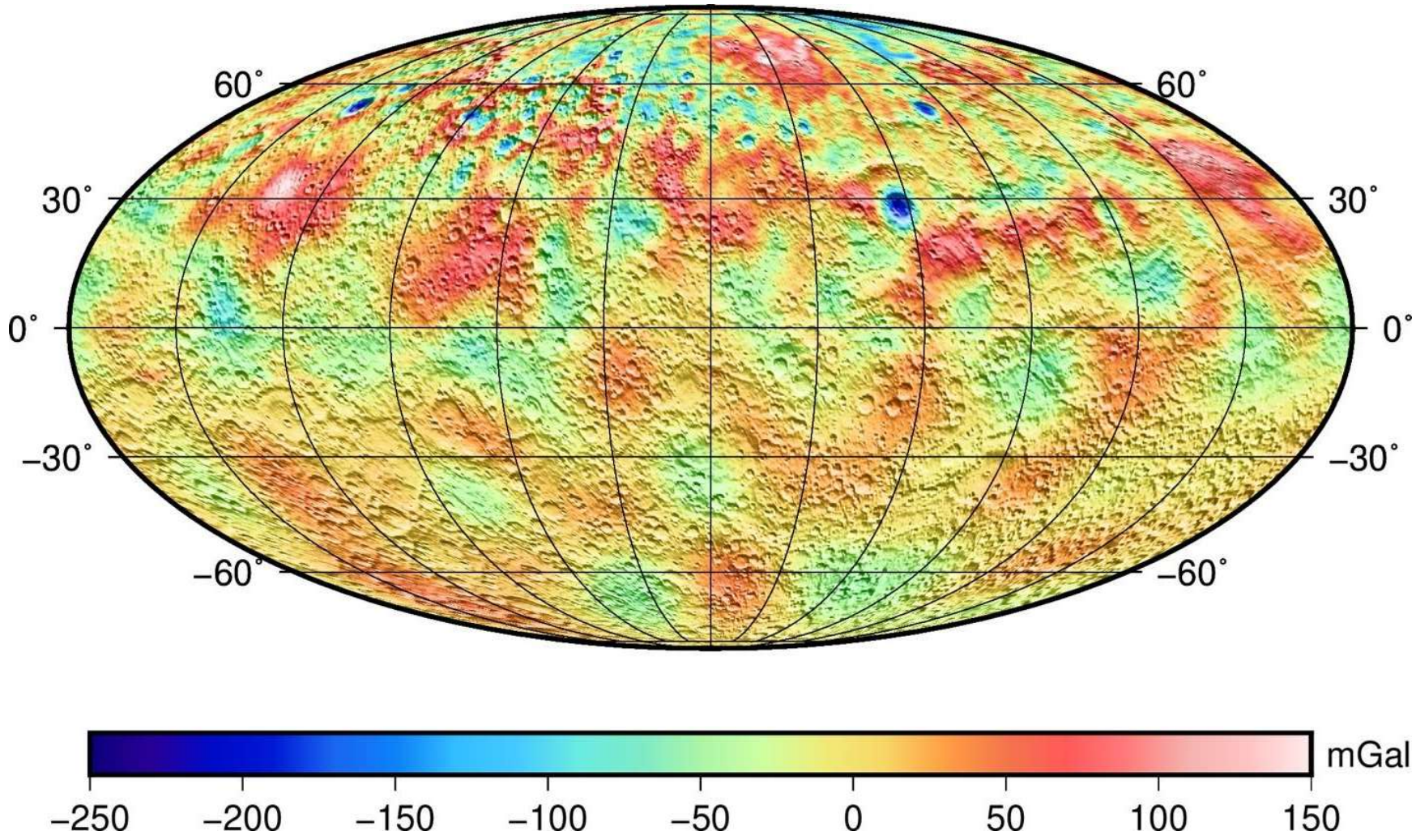

Figure S2 Global map of the free-air gravity anomaly (mGal) from the gravity field retrieved by constraining the measured acceleration profiles with the degree strength technique [3] in a Mollweide projection centered on 0° longitude. The shaded topographic relief in this figure and figures S3 and S4 is based on the U.S. Geological Survey (USGS) map by [4].

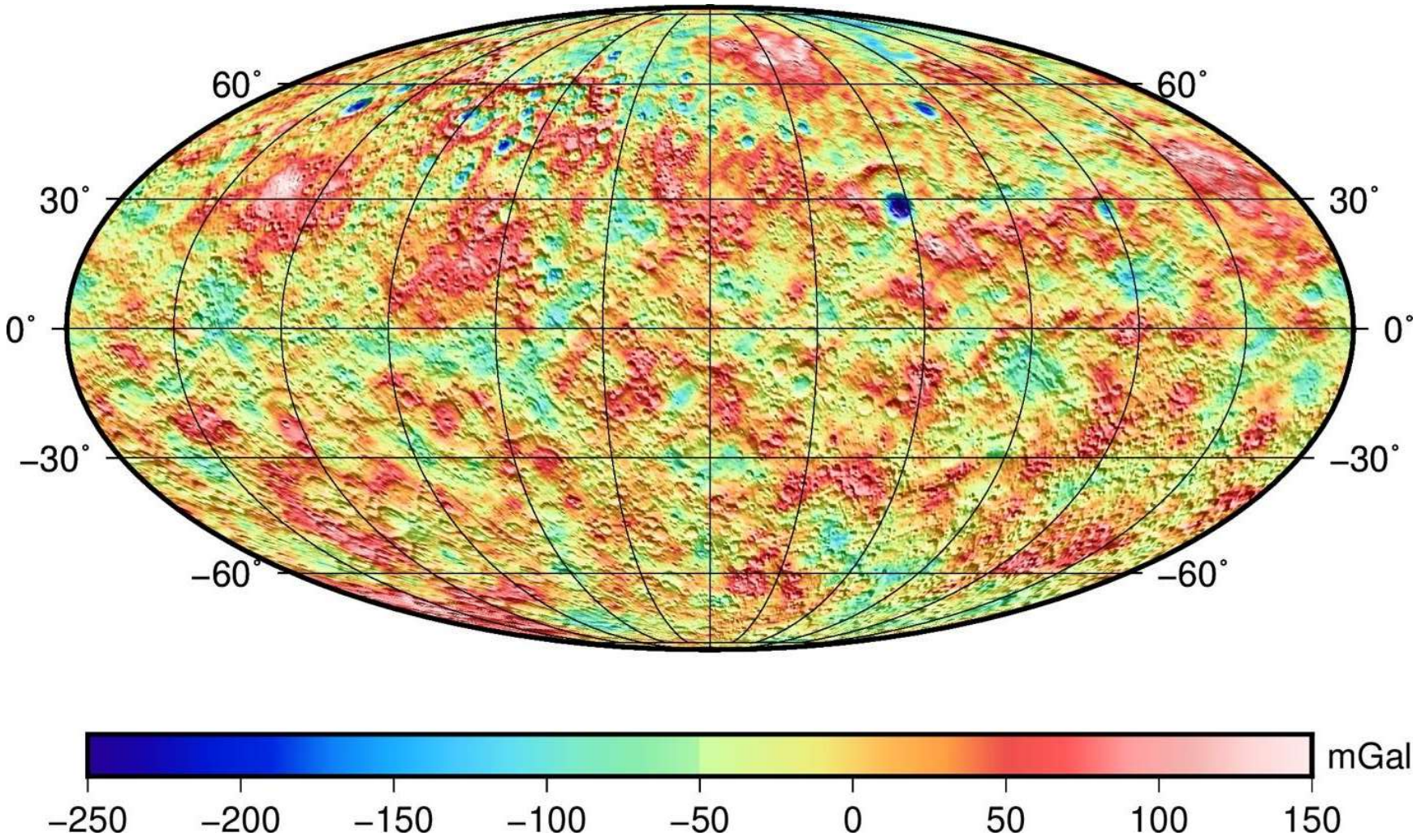

Figure S3 Global map of the free-air gravity anomaly (mGal) from our gravity solution retrieved by constraining the harmonic degrees greater than 10 with the power spectrum associated with gravity from topography [4] in a Mollweide projection centered on 0° longitude. These *a priori* formal uncertainties were computed by assuming a density crust of ρ_c = 2800 kg m^{-3}.

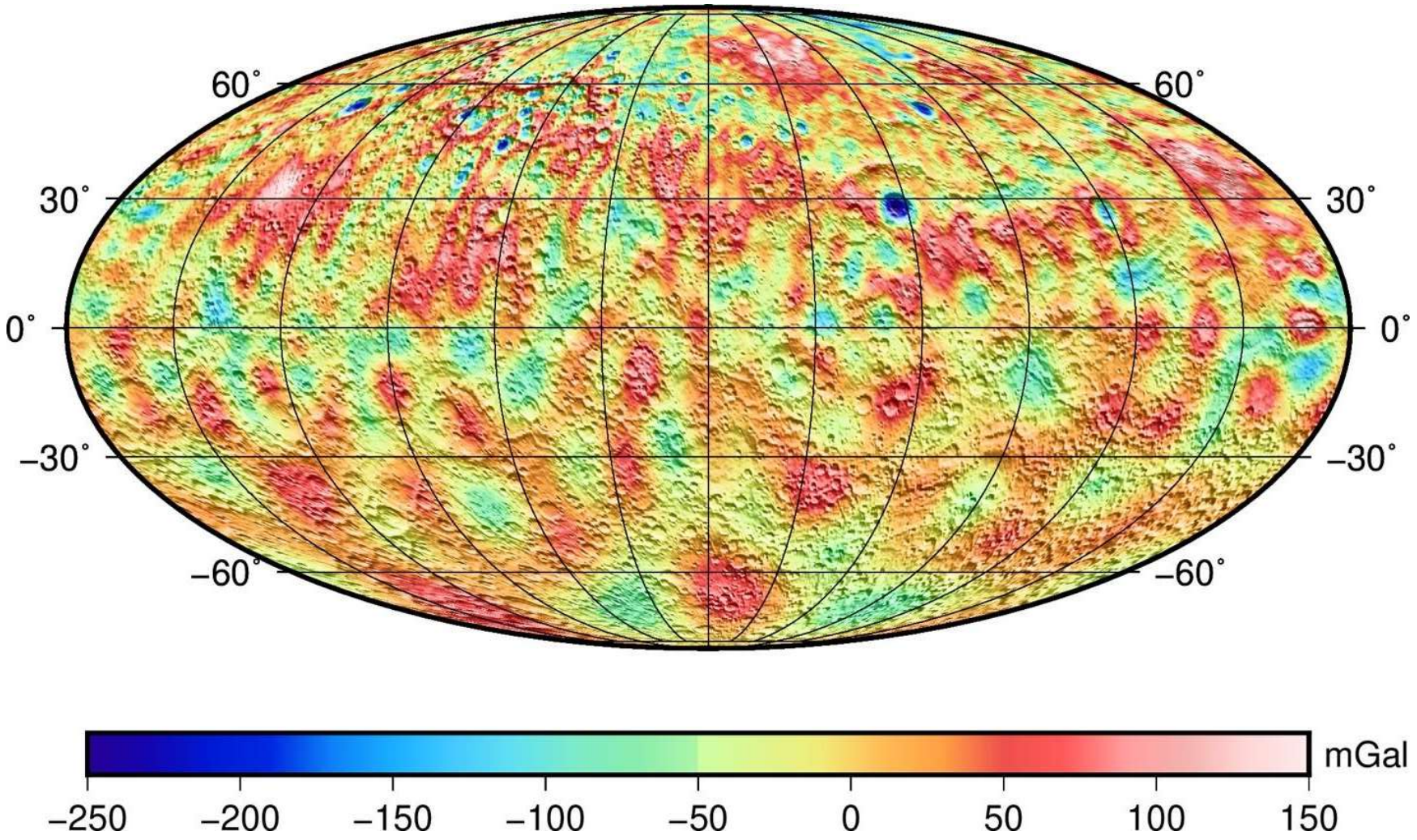

Figure S4 Global map of the free-air gravity anomaly (mGal) from gravity field *HgM009* in a Mollweide projection centered on 0° longitude. The shaded topographic relief is based on the (USGS) map by [4].

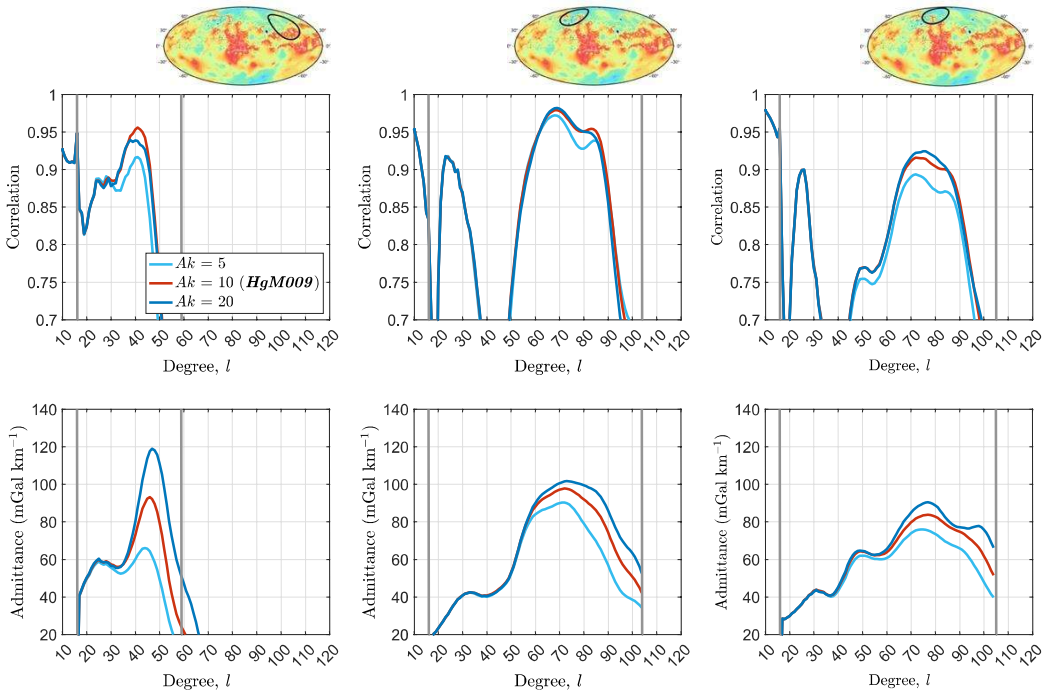

Figure S5 Gravity/topography local correlation and admittance spectra on a spherical cap centered at (**left**) 38°N-latitude and 110°E-longitude, (**center**) 60°N-latitude and 290°E-longitude, and (**right**) 64°N-latitude and 319°E-longitude. These profiles are obtained by assuming a spherical cap radius of 20°, a concentration factor of 99.9%, and a spherical harmonic expansion l_{max} based on the degree strength map (Figure S1). Each localized spectral admittance is computed with a gravity field determined by using the Kaula constraint with a scale factor Ak equal to 5 (**cyan**), 10 (**blue**) and 20 (**red**). Vertical gray lines show the degrees range between L_{win} and $l_{max} - L_{win}$.

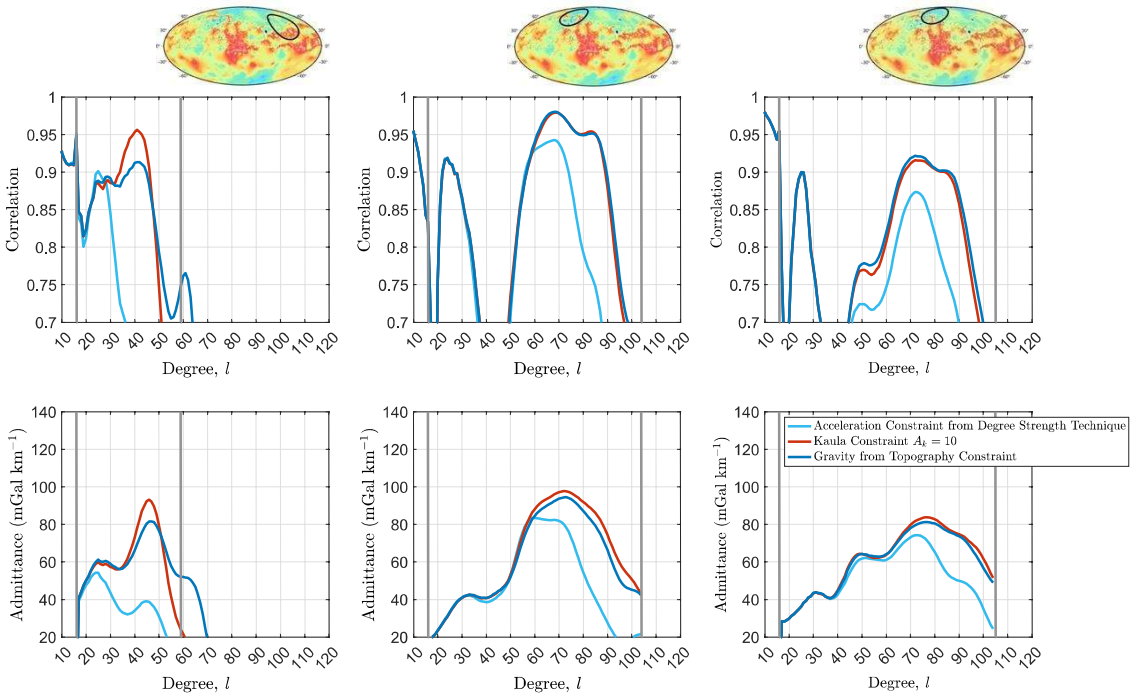

Figure S6 Gravity/topography local correlation and admittance spectra on a spherical cap centered at (**left**) 38°N-latitude and 110°E-longitude, (**center**) 60°N-latitude and 290°E-longitude, and (**right**) 64°N-latitude and 319°E-longitude. These profiles are obtained by assuming a spherical cap radius of 20˚, a concentration factor of 99.9%, and a spherical harmonic expansion l_{max} based on the degree strength map (Figure S1). Each localized spectral admittance is computed with a gravity field determined by using the Kaula constraint with Ak equal to 5 (**red**), acceleration constraint based on the degree strength technique (**cyan**) and gravity from topography constraint (**blue**). Vertical gray lines show the degrees range between L_{win} and $l_{max} - L_{win}$.

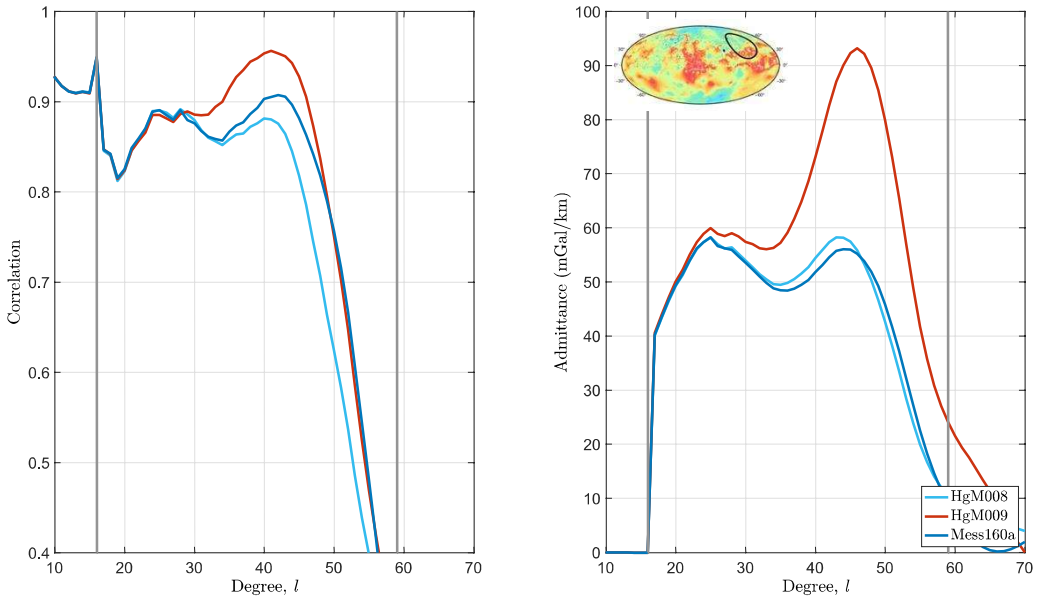

Figure S7 Gravity/topography (**left**) correlation and (**right**) admittance spectra on a local spherical cap centered at 38°N-latitude and 110°E-longitude with a radius of 20°, a concentration factor of 99.9%. The gravity fields used in this localized admittance analysis are HgM008 (**cyan**) [5], HgM009 (**red**) and Mess160a (**blue**) [6]. Vertical gray lines show the degrees range between L_{win} and $l_{max} - L_{win}$, which is equal to l_{DS}=59 (Figure S1).

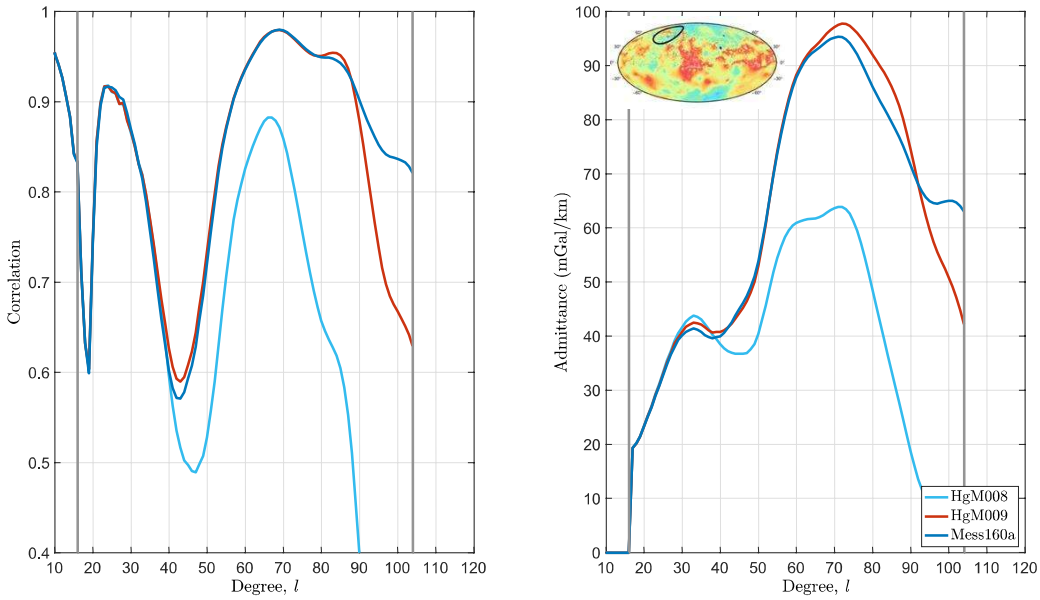

Figure S8 Gravity/topography (**left**) correlation and (**right**) admittance spectra on a local spherical cap centered at 60°N-latitude and 290°E-longitude with a radius of 20˚, a concentration factor of 99.9%. The gravity fields used in this localized admittance analysis are HgM008 (**cyan**) [5], HgM009 (**red**) and Mess160a (**blue**) [6]. Vertical gray lines show the degrees range between L_{win} and $l_{max} - L_{win}$, which is equal to l_{DS}=104 (Figure S1).

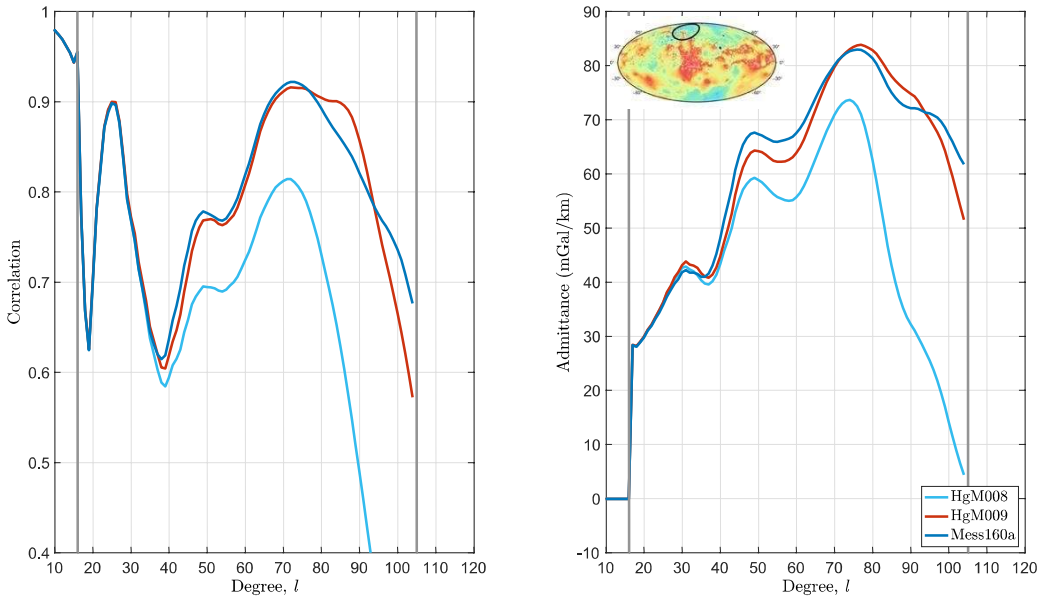

Figure S9 Gravity/topography (**left**) correlation and (**right**) admittance spectra on a local spherical cap centered at 64°N-latitude and 319°E-longitude with a radius of 20˚, a concentration factor of 0.999. The gravity fields used in this localized admittance analysis are HgM008 (**cyan**) [5], HgM009 (**red**) and Mess160a (**blue**) [6]. Vertical gray lines show the degrees range between L_{win} and $l_{max} - L_{win}$, which is equal to l_{DS}=105 is given by the degree strength map (Figure S1).

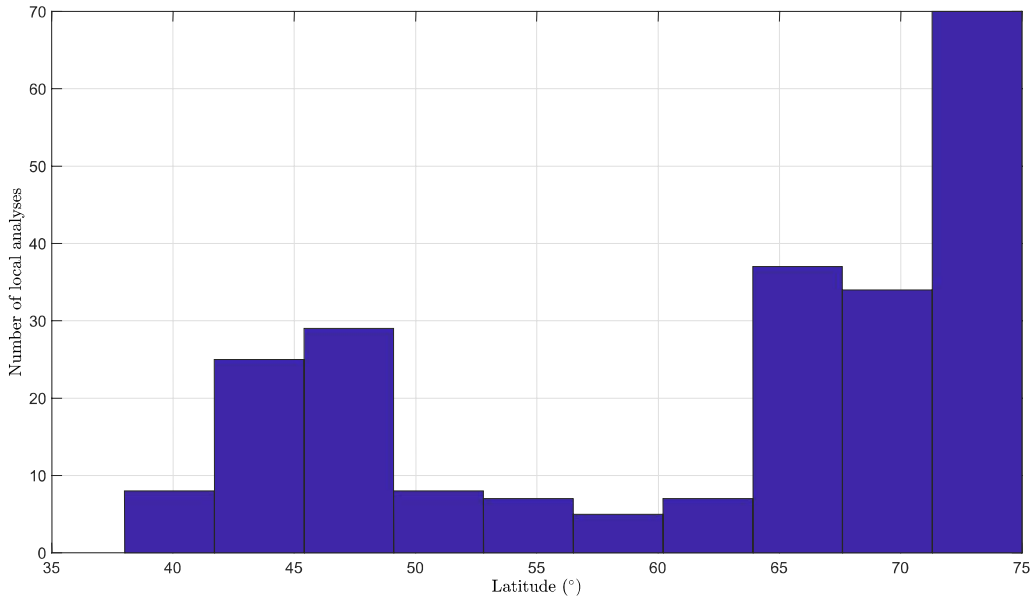

Figure S10 Histogram of the local spherical cap center latitude of the 230 analyses that met the requirement $RMS_{misfit} < \bar{\sigma}$. The 65% of these analyses are above 60°N-latitude, where the resolution of Mercury's gravity field is higher.

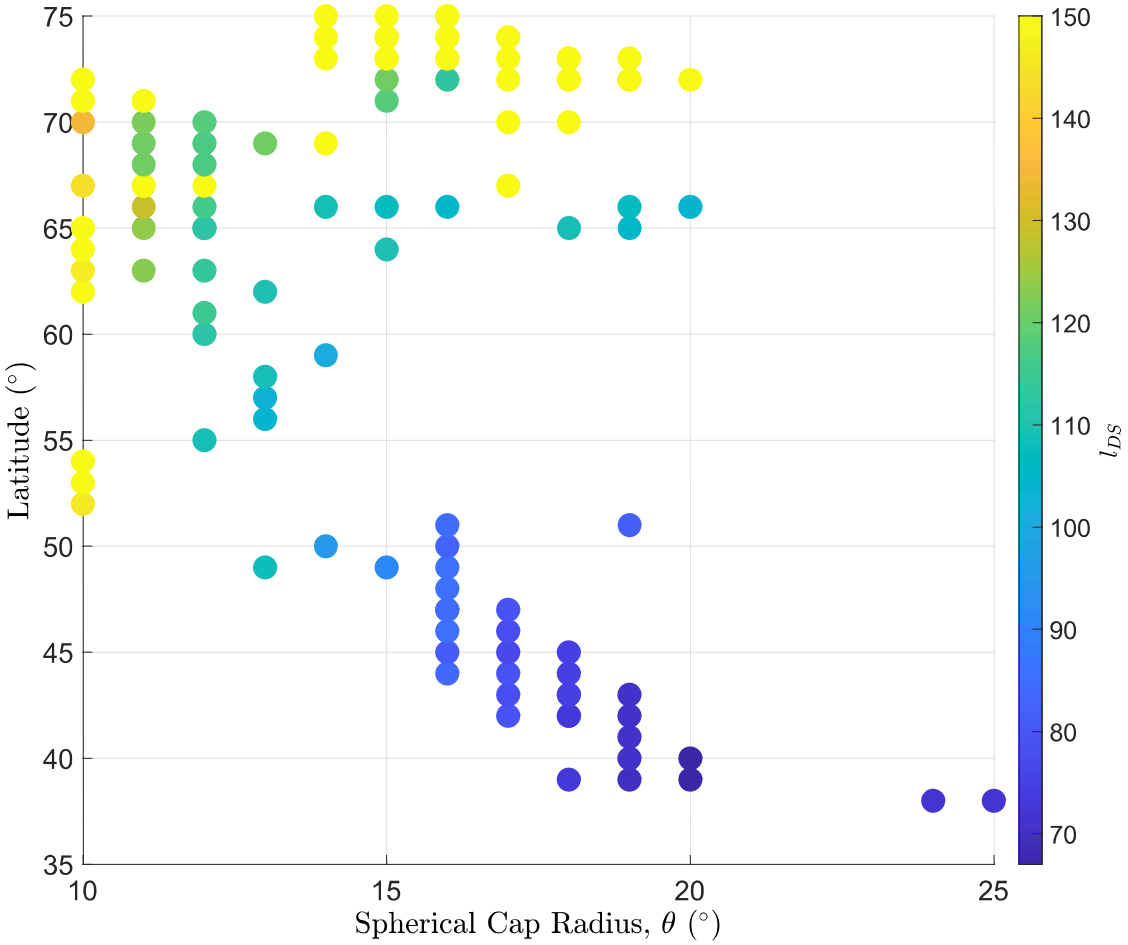

Figure S11 Radius (θ) and center latitude of the spherical cap windowing of the 230 admittance spectra that fit the localized admittance predicted by a spherical shell model based on surface loads [2]. Colors show the spherical harmonic expansion of the gravity field, l_{DS}, based on the degree strength map (Figure S1).

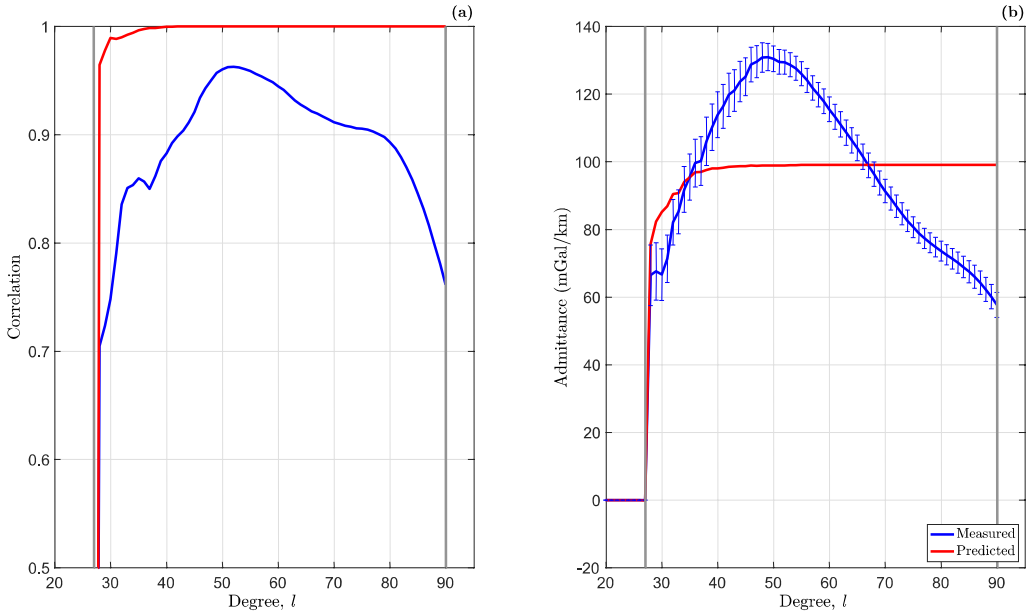

Figure S12 Gravity/topography (**a**) correlation and (**b**) admittance spectra on a local spherical cap centered at 45N-latitude and 15E-longitude with a radius of 12˚, a concentration factor of 99.9%. Red lines are the correlation and admittance spectra predicted by the top loading model (presented in Section 2.3) that provides the best fit with the observed admittance. Vertical gray lines show the degrees range between L_{win} and $l_{max} - L_{win} = l_{DS}$, where l_{DS} is based on the degree strength map (Figure S1).

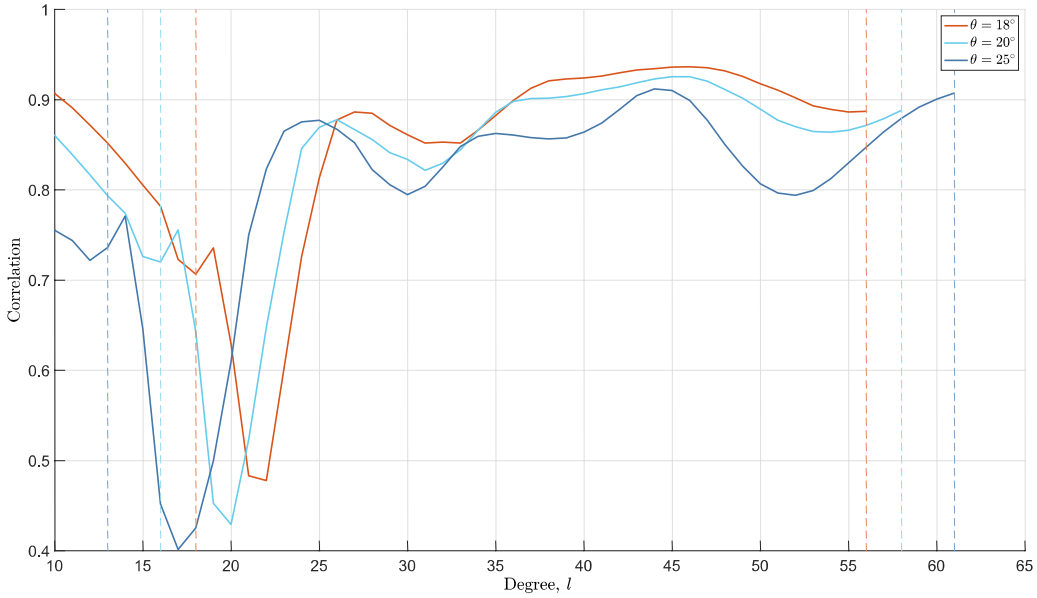

Figure S13 Correlations between gravity and topography localized on a spherical cap with varying radii (θ) of $18°, 20°$, and $25°$. Each localization windowing is carried out with a concentration factor of 99.9% that leads to $L_{win} = 18$, 16 and 13 for $\theta = 18°, 20°$, and $25°$, respectively. Dashed lines show the range of investigated range of degrees between L_{win} and $l_{max} - L_{win} = l_{DS}$, where l_{DS} is based on the degree strength map (Figure S1).

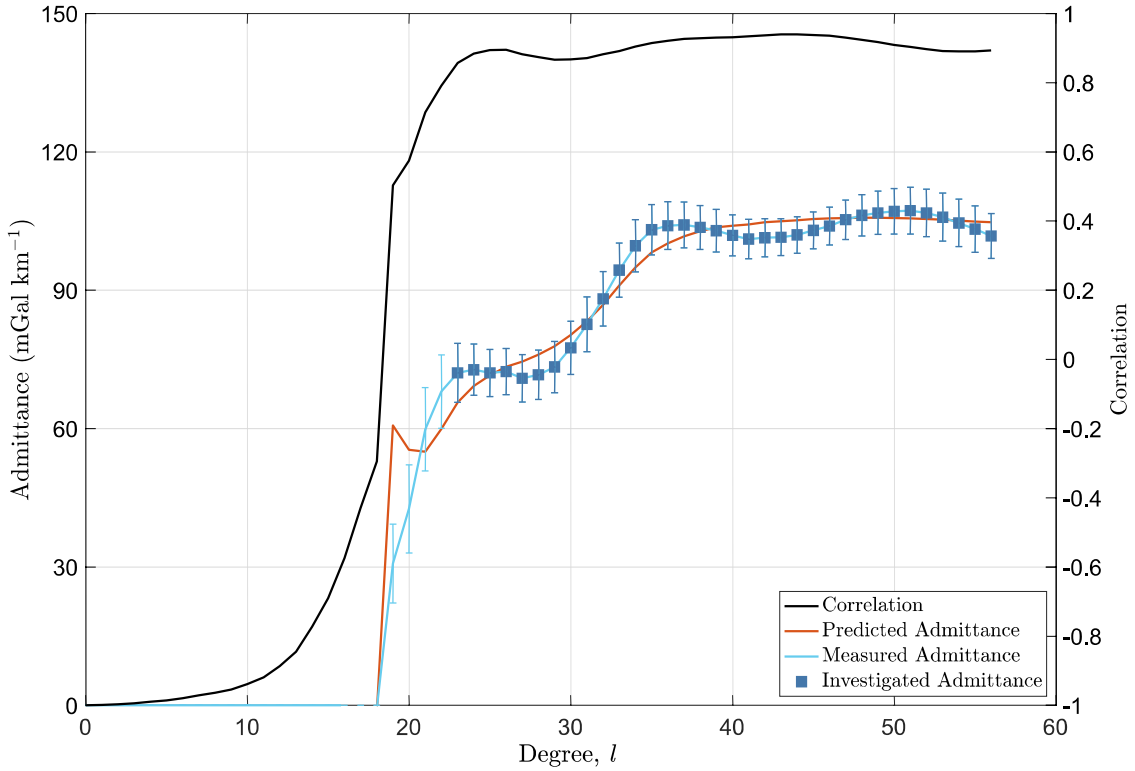

Figure S14 Correlation and admittance spectra of the gravity and topography localized on a spherical cap centered at 286ºE longitude and 44ºN latitude. The details of the localization windowing are presented in the caption of Fig. 3. The predicted admittance is based on synthetic gravity fields that are computed by assuming top/bottom loads modeling (e.g., [1]).

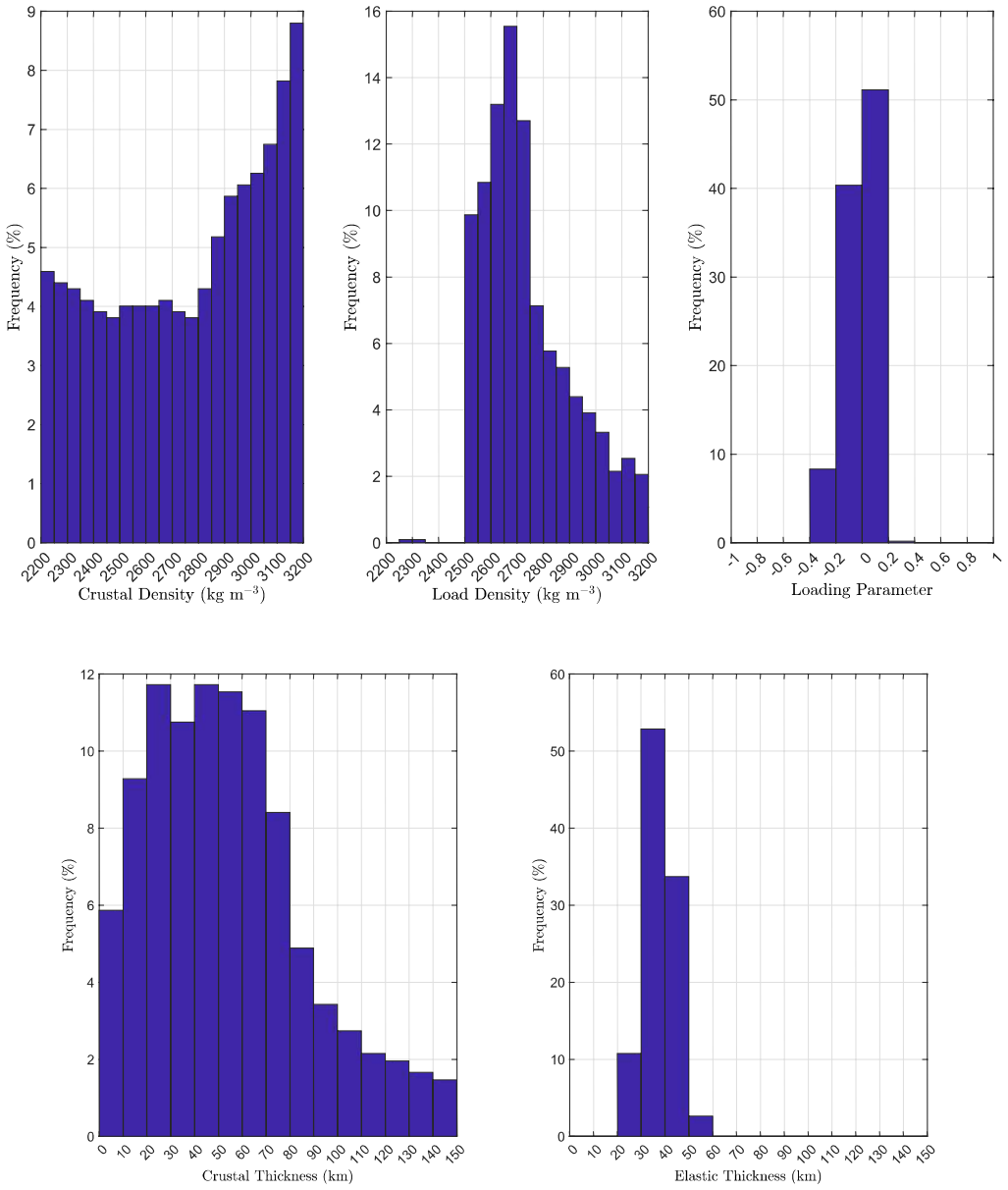

Figure S15 Histograms for the parameters of interest that are estimated through the admittance analysis of gravity and topography localized on the spherical cap described in the caption of Fig. 3. The predicted admittance spectrum is based on the top loads modeling as discussed in Sec. 4. The estimates of these parameters are: crustal density $\rho_c = 2762 \pm 296$ kg m^{-3}; load density $\rho_l = 2670 \pm 160$ kg m^{-3}; loading parameter $L = -0.08 \pm 0.12$; crustal thickness $T_c = 51 \pm 37$ km; and elastic thickness $T_e = 32 \pm 6$ km.

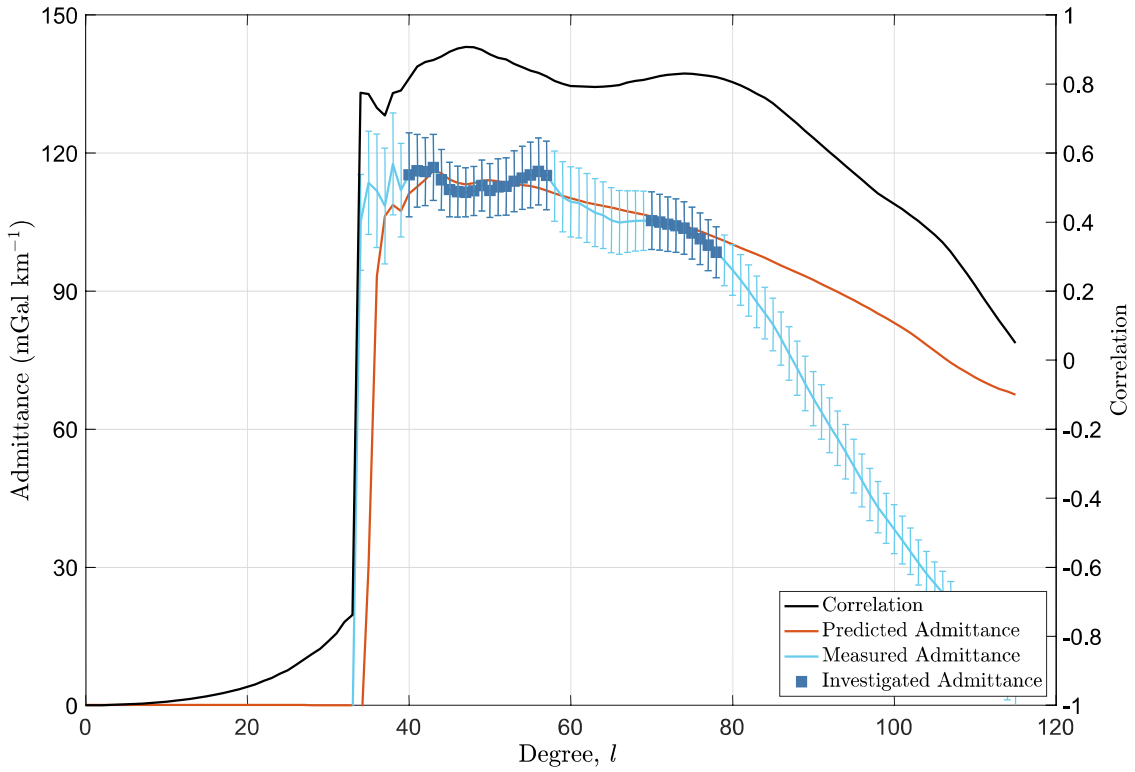

Figure S16 Correlation and admittance spectra of gravity and topography localized on a spherical cap centered at 53°E longitude and 4°N latitude. The details of the localization windowing are presented in the caption of Fig. 5. The predicted admittance is based on synthetic gravity fields that are computed by assuming top/bottom loads modeling (*e.g.*, [1]).

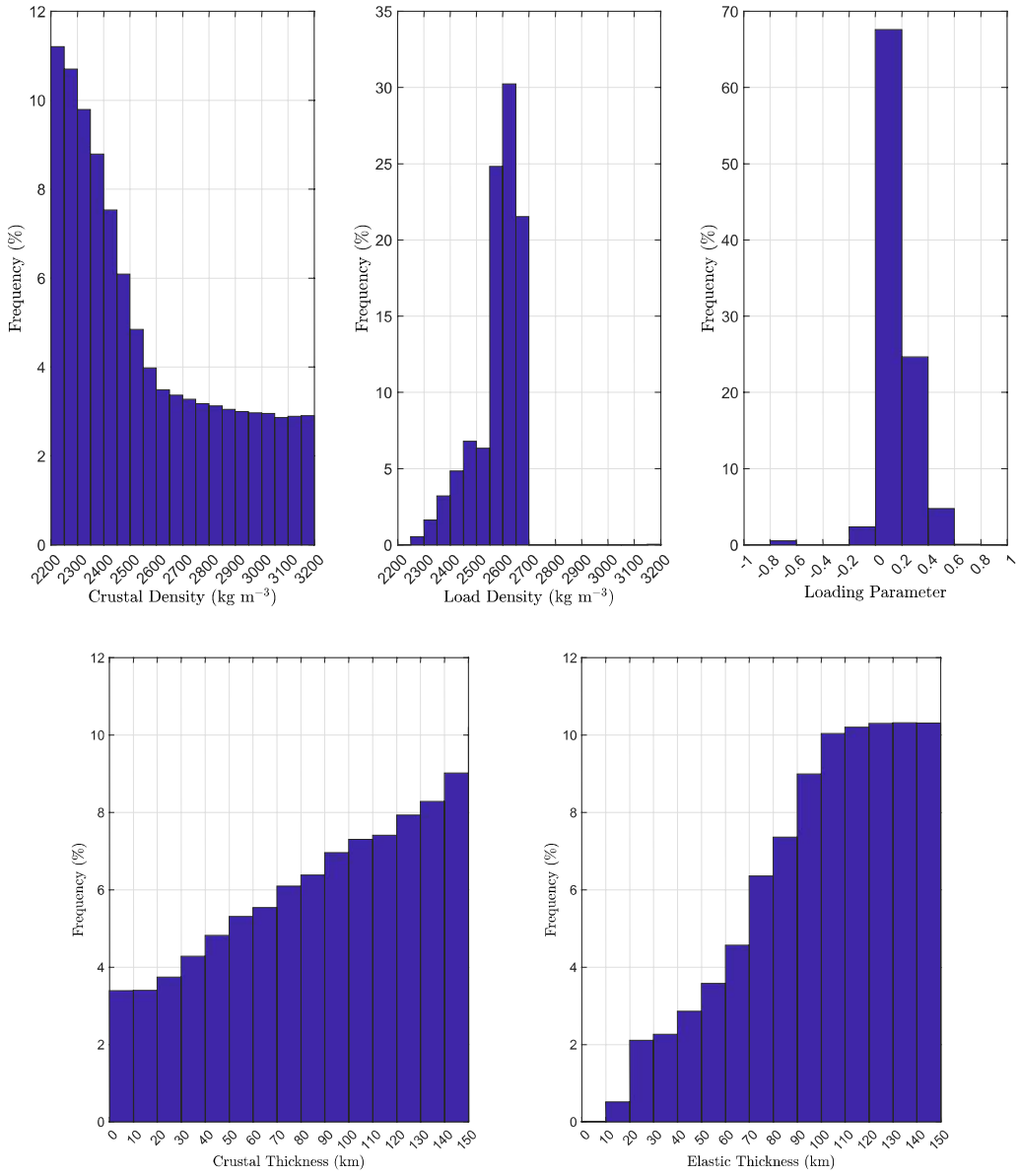

Figure S17 Histograms for the parameters of interest that are estimated through the admittance analysis of gravity and topography localized on the spherical cap described in the caption of Fig. 5. The predicted admittance spectrum is based on the top loads modeling as discussed in Sec. 4. The estimates of these parameters are: $\rho_c = 2534 \pm 288$ kg m^{-3}; $\rho_l = 2558 \pm 88$ kg m^{-3}; $L = 0.06 \pm 0.14$; $T_c = 90 \pm 45$ km; and $T_e = 102 \pm 35$ km.

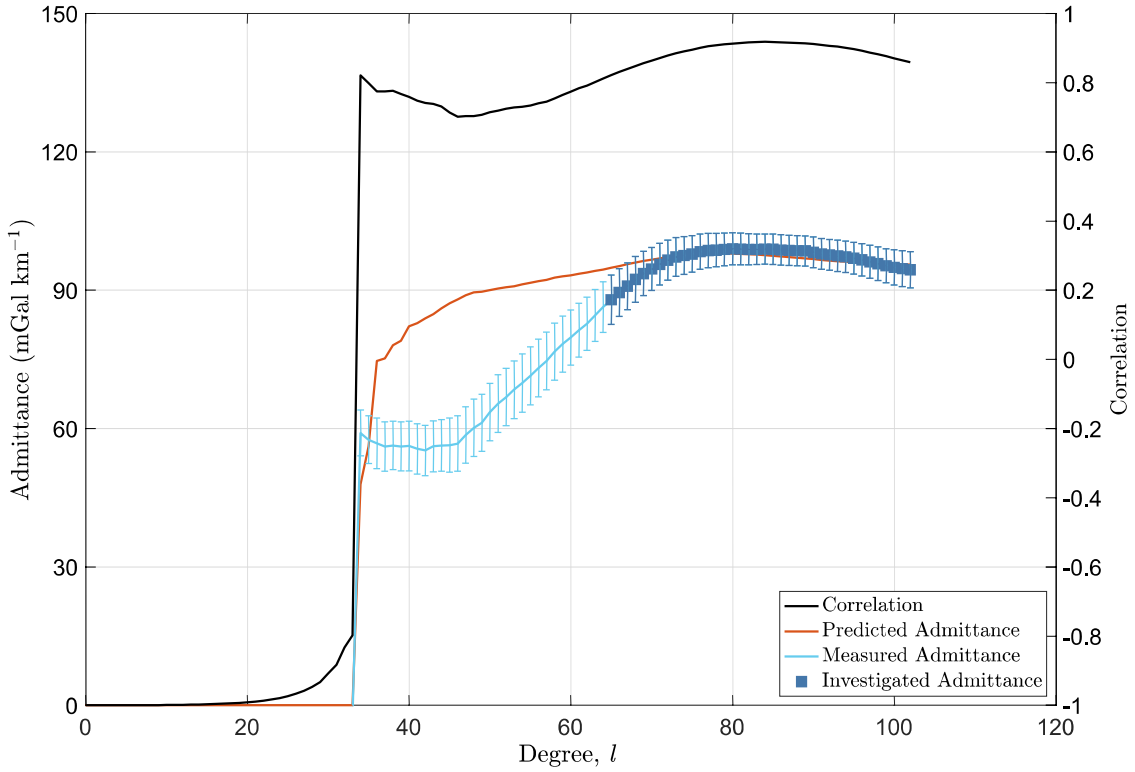

Figure S18 Correlation and admittance spectra of gravity and topography localized on a spherical cap centered at 303ºE longitude and 70ºN latitude. The details of the localization windowing are presented in the caption of Fig. 7. The predicted admittance is based on synthetic gravity fields that are computed by assuming top/bottom loads modeling (*e.g.*, [1]).

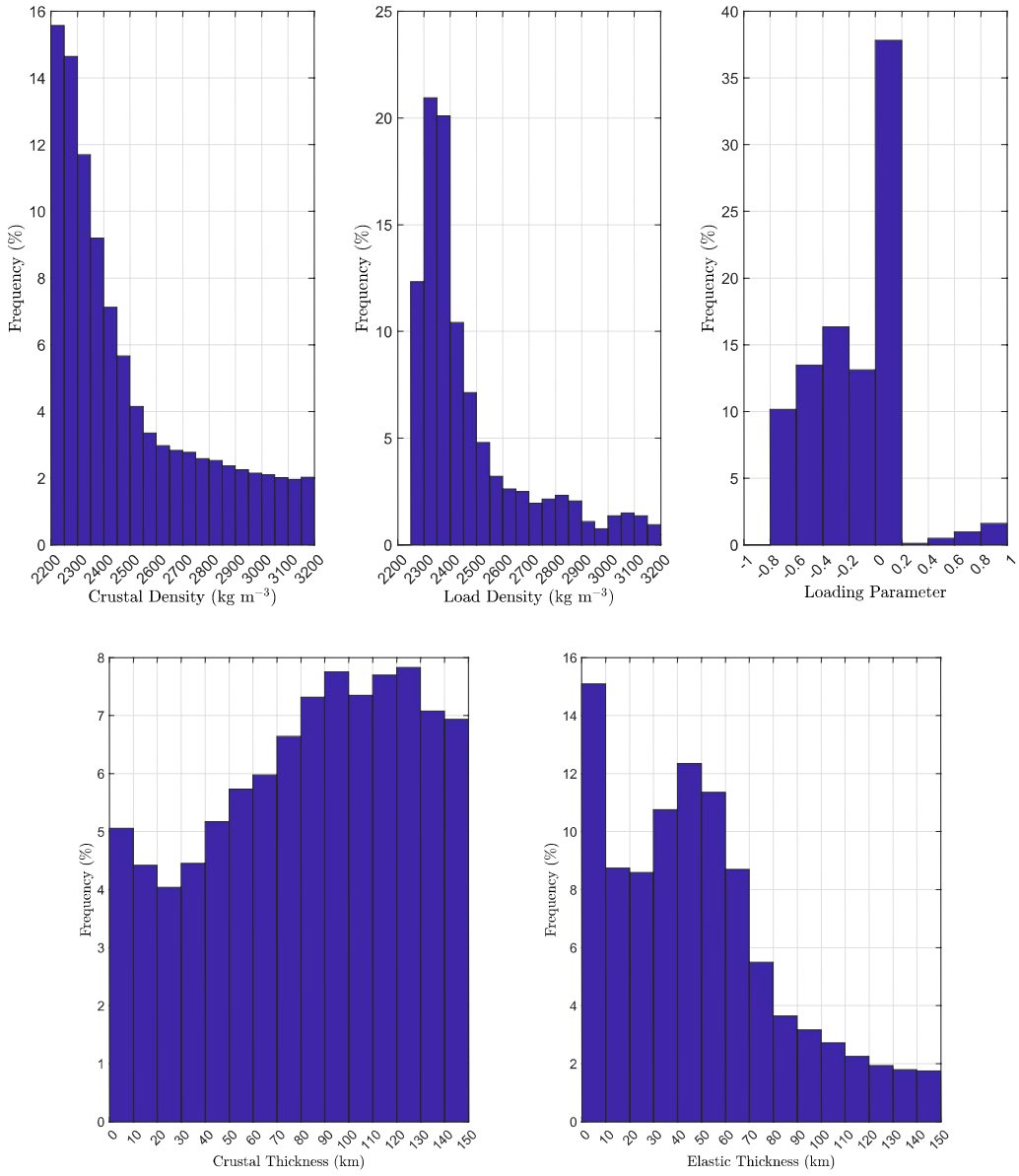

Figure S19 Histograms for the parameters of interest that are estimated through the admittance analysis of gravity and topography localized on the spherical cap described in the caption of Fig. 5. The predicted admittance spectrum is based on the top loads modeling as discussed in Sec. 4. The estimates of these parameters are: $\rho_c = 2472 \pm 272\,\mathrm{kg\,m^{-3}}$; $\rho_l = 2455 \pm 223\,\mathrm{kg\,m^{-3}}$; $L = -0.17 \pm 0.43$; $T_c = 83 \pm 44$ km; and $T_e = 46 \pm 38$ km.

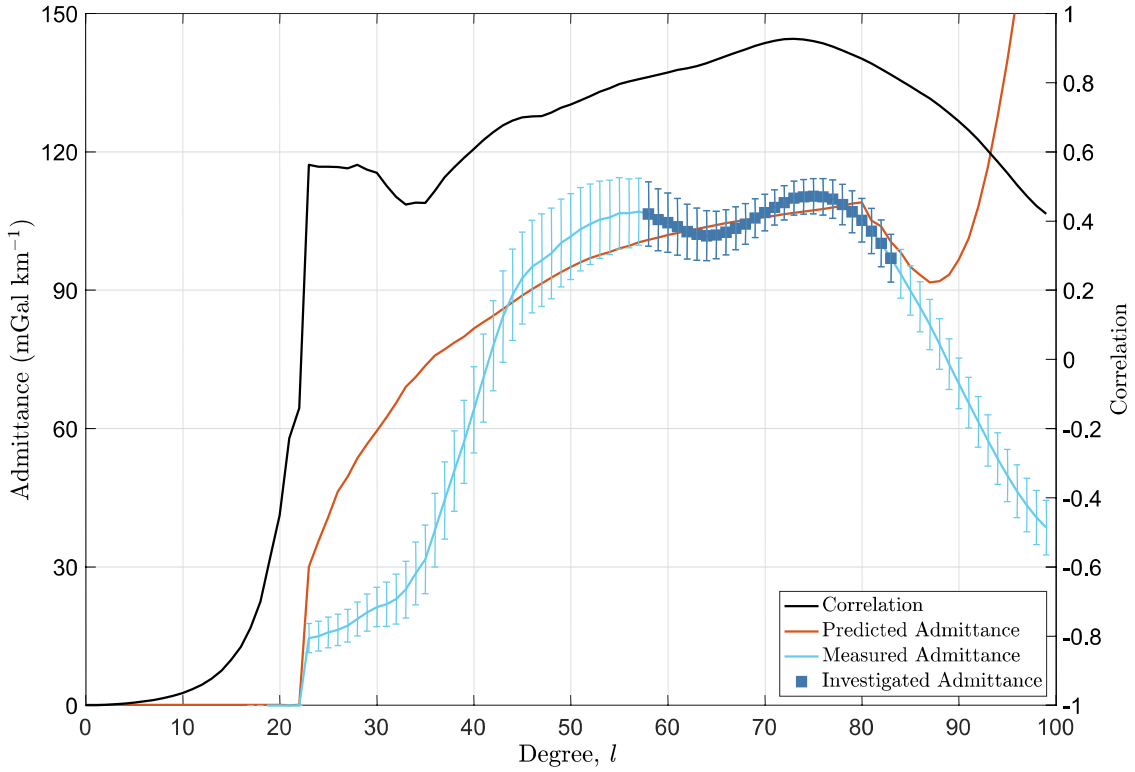

Figure S20 Correlation and admittance spectra of gravity and topography localized on a spherical cap centered at 250ºE longitude and 72ºN latitude. The details of the localization windowing are presented in the caption of Fig. 9. The predicted admittance is based on synthetic gravity fields that are computed by assuming top/bottom loads modeling (*e.g.*, [1]).

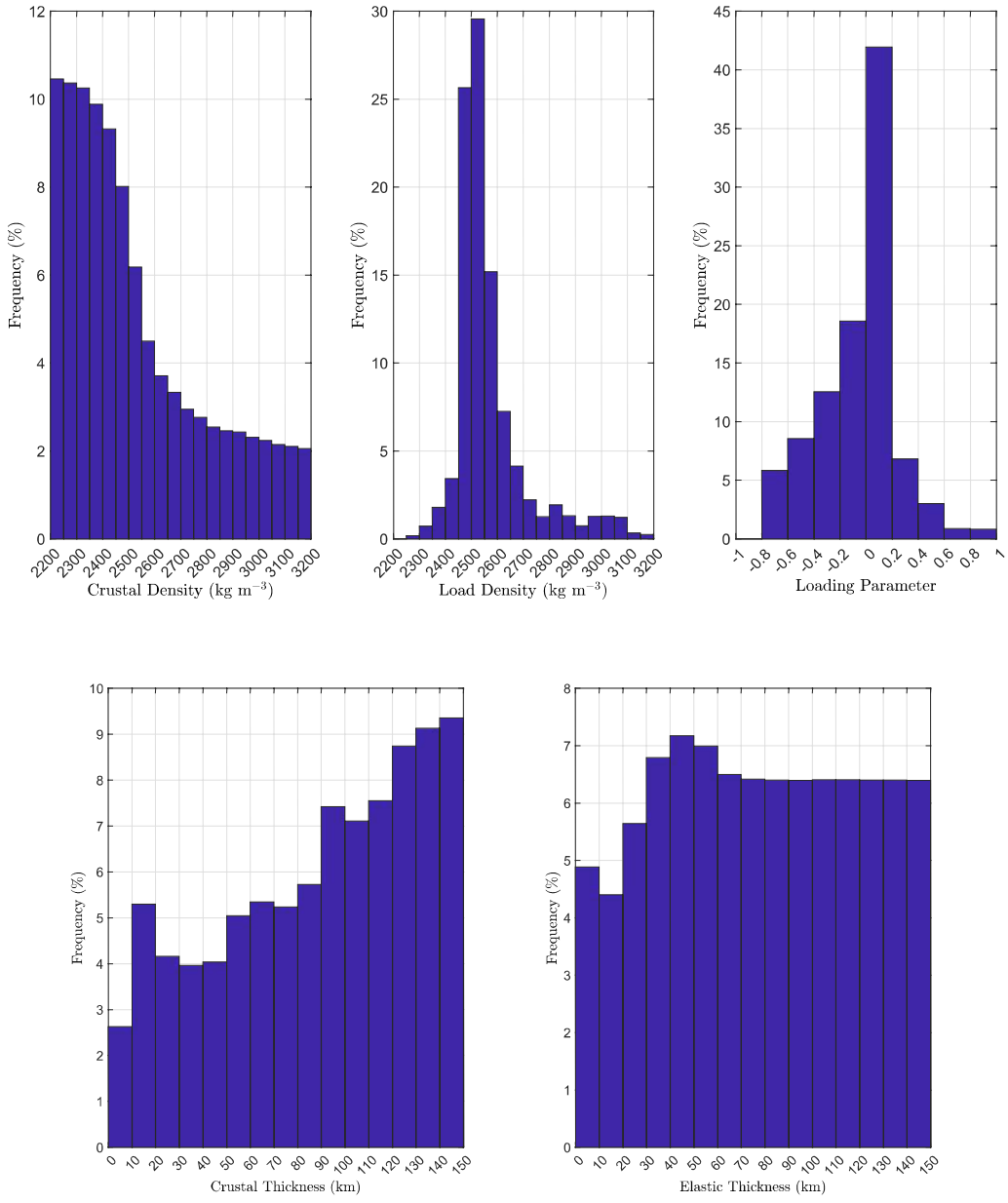

Figure S21 Histograms for the parameters of interest that are estimated through the admittance analysis of gravity and topography localized on the spherical cap described in the caption of Fig. 5. The predicted admittance spectrum is based on the top loads modeling as discussed in Sec. 4. The estimates of these parameters are: $\rho_c = 2652 \pm 290$ kgm^{-3}; $\rho_l = 2542 \pm 125$ kgm^{-3}; $L = -0.26 \pm 0.31$; $T_c = 98 \pm 41$ km; and $T_e = 77 \pm 45$ km.

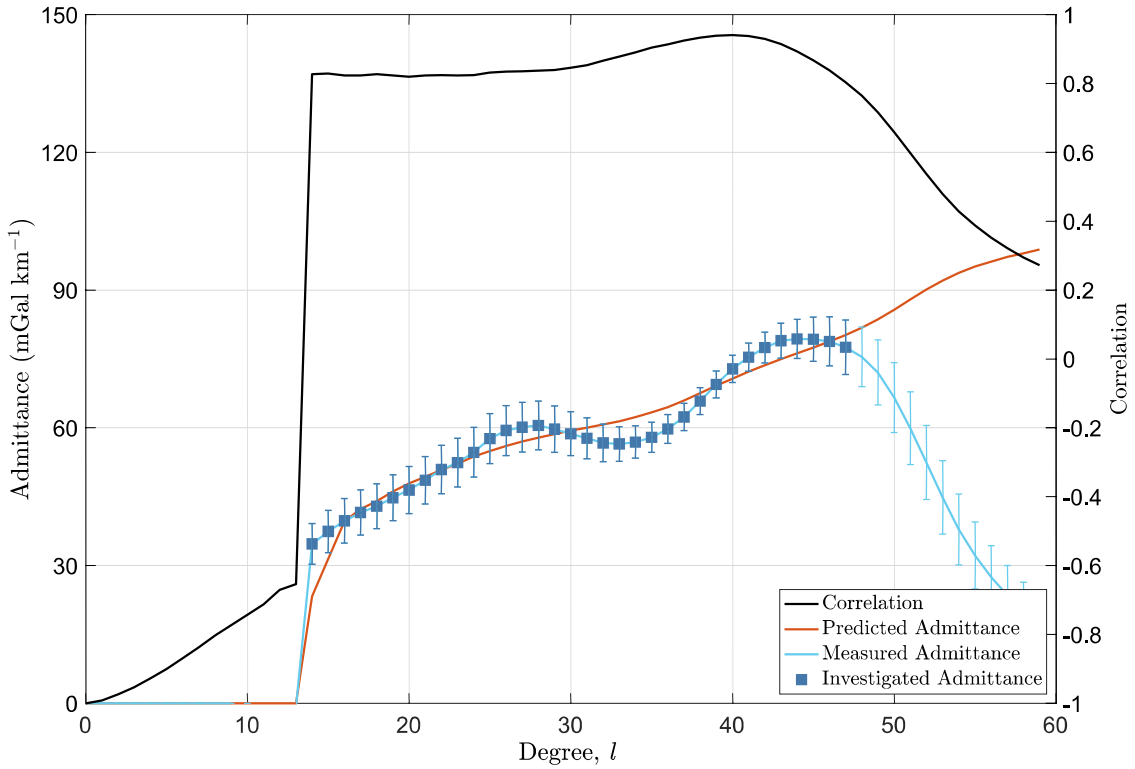

Figure S22 Correlation and admittance spectra of gravity and topography localized on a spherical cap centered at 110ºE longitude and 38ºN latitude. The details of the localization windowing are presented in the caption of Fig. 11. The predicted admittance is based on synthetic gravity fields that are computed by assuming top/bottom loads modeling (*e.g.*, [1]).

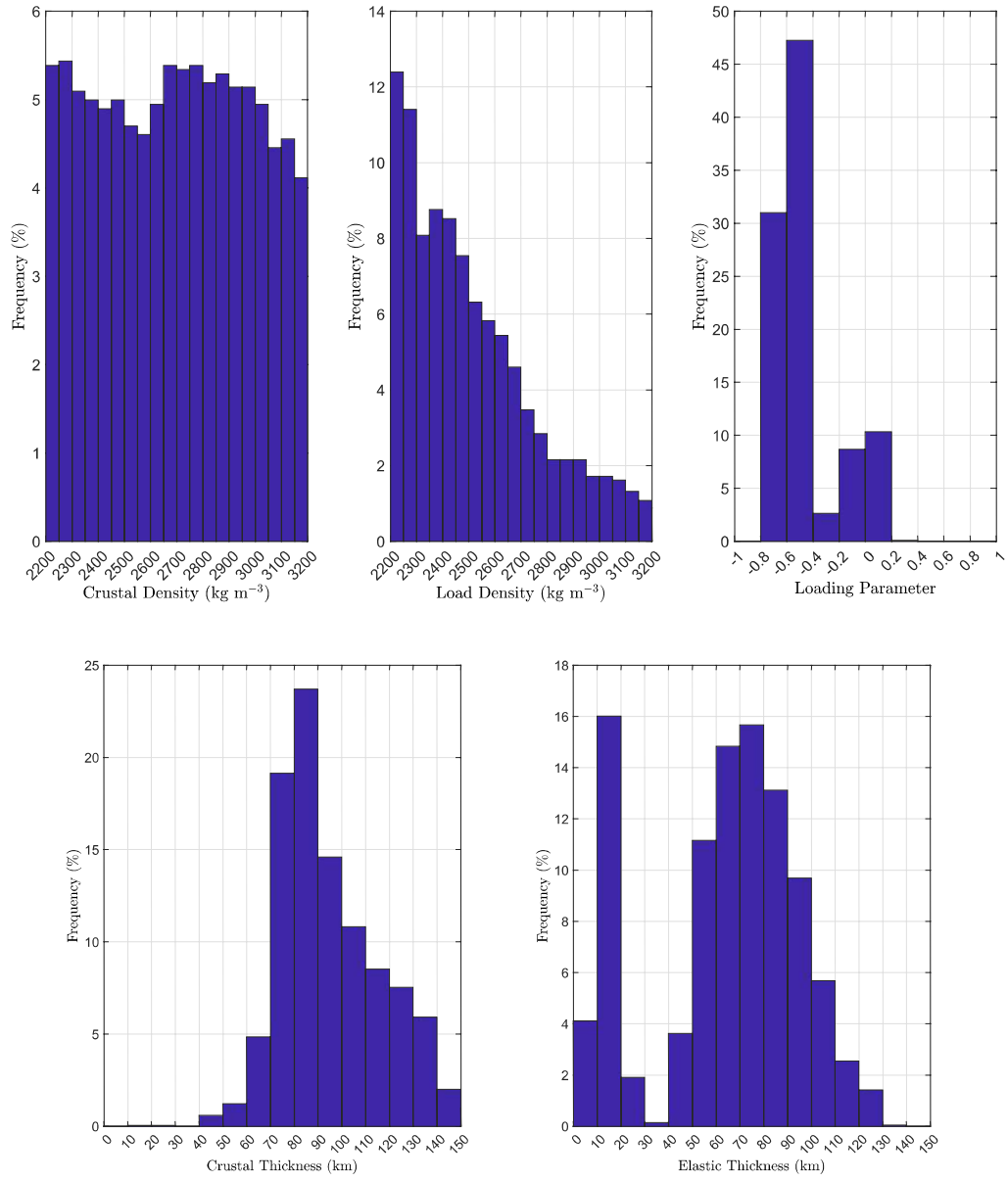

Figure S23 Histograms for the parameters of interest that are estimated through the admittance analysis of gravity and topography localized on the spherical cap described in the caption of Fig. 11. The predicted admittance spectrum is based on the top loads modeling as discussed in Sec. 4. The estimates of these parameters are: $\rho_c = 2665 \pm 285\,\mathrm{kg m^{-3}}$; $\rho_l = 2490 \pm 252\,\mathrm{kg m^{-3}}$; $L = -0.56 \pm 0.25$; $T_c = 91 \pm 22\,\mathrm{km}$. The elastic thickness shows a bimodal probability distribution with two peaks at 15 km and 75 km, respectively.

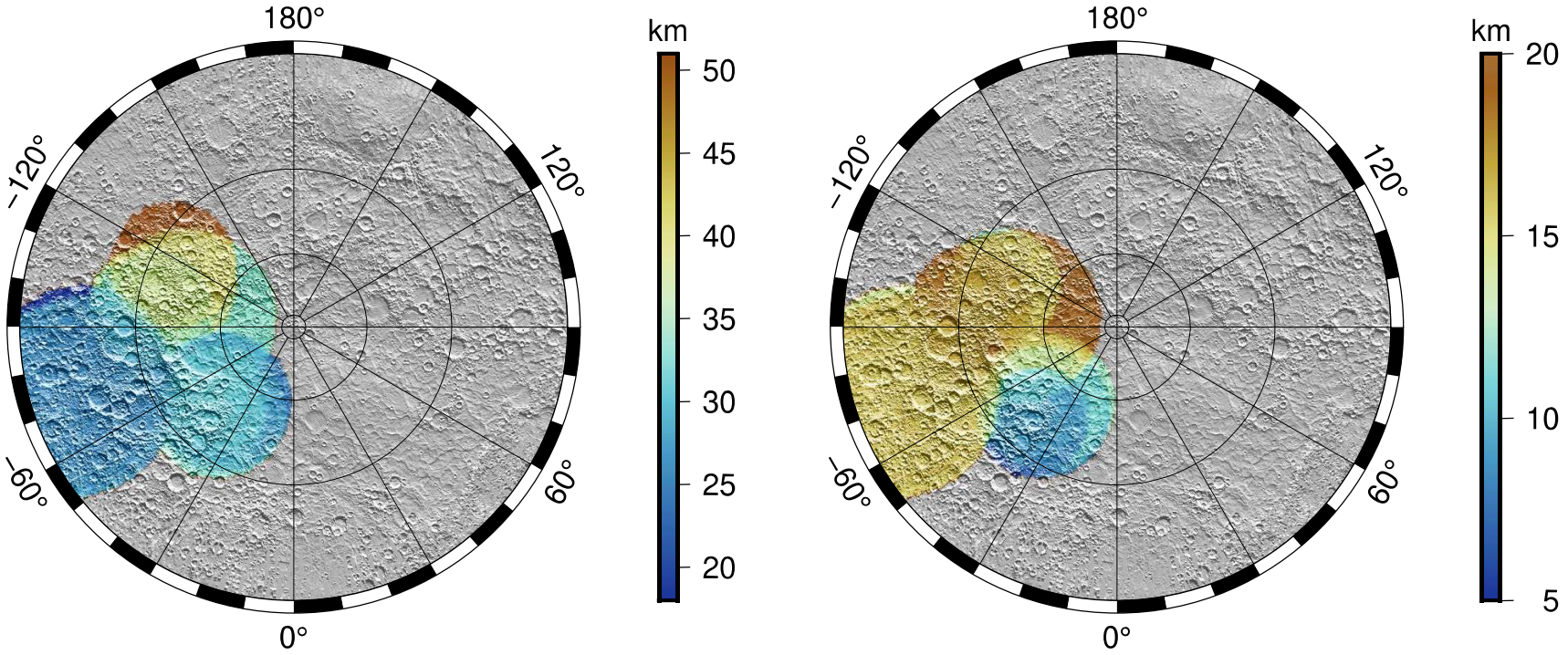

Figure S24 Maps of the lateral variations of the (**left**) crustal thickness and (**right**) its uncertainty in a polar stereographic projection from 30ºN-latitude. This map is obtained by assuming surface loads only. Grey colors show regions where the localized admittance spectra do not allow to constrain the crustal density.

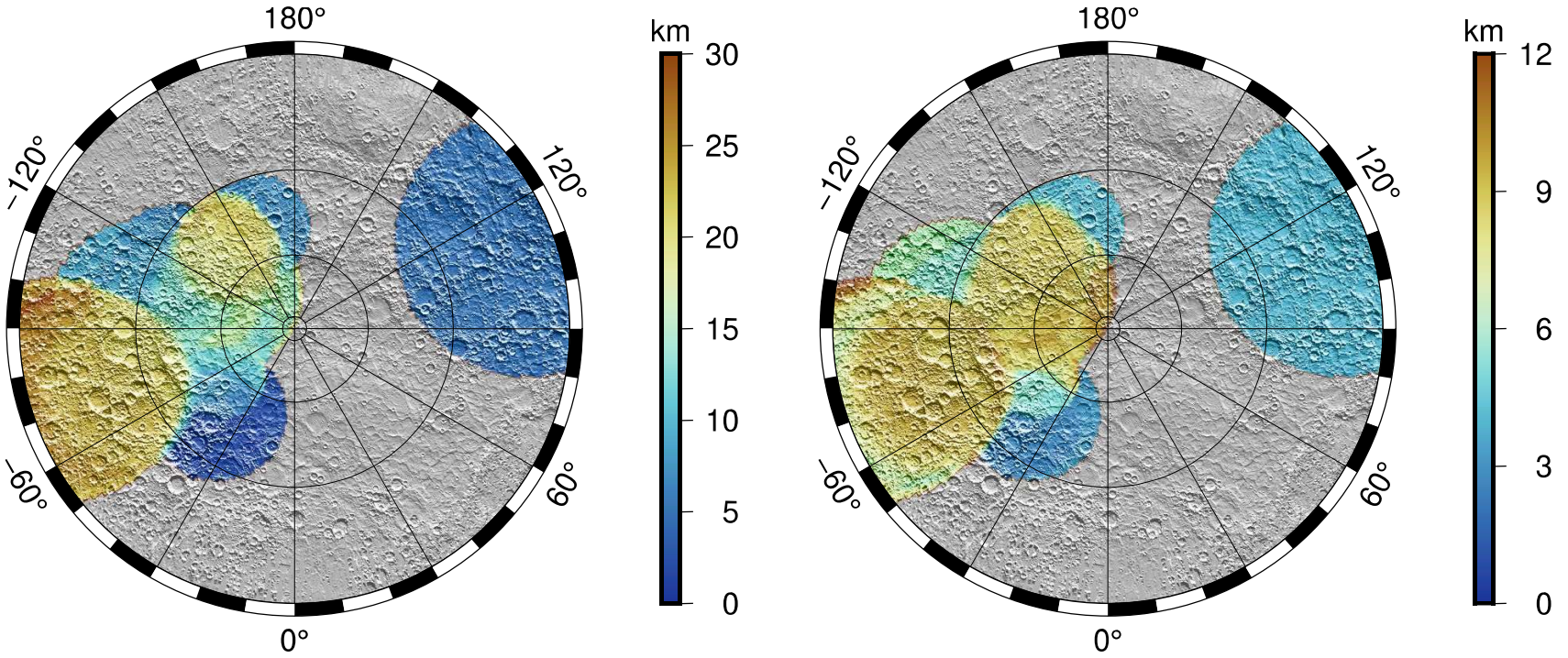

Figure S25 Maps of the lateral variations of the (**left**) elastic thickness and (**right**) its uncertainty in a polar stereographic projection from 30ºN-latitude. This map is obtained by assuming surface loads only. Grey colors show regions where the localized admittance spectra do not allow to constrain the crustal density.

Supplementary References

[1] Broquet, A., and M. A. Wieczorek. 2019. "The Gravitational Signature of Martian Volcanoes." *Journal of Geophysical Research: Planets* 124 (8): 2054–86. https://doi.org/10.1029/2019JE005959.

[2] Turcotte, D. L., R. J. Willemann, W. F. Haxby, and John Norberry. 1981. "Role of Membrane Stresses in the Support of Planetary Topography." *Journal of Geophysical Research: Solid Earth* 86 (B5): 3951–59. https://doi.org/10.1029/JB086IB05P03951

[3] Konopliv, A. S., W. B. Banerdt, and W. L. Sjogren, "Venus Gravity: 180th Degree and Order Model," *Icarus*, vol. 139, no. 1, pp. 3–18, May 1999, doi: 10.1006/ICAR.1999.6086.

[4] Becker, K. J., *et al.*, "First global digital elevation model of Mercury," 2016.

[5] Genova, A., S. Goossens, E. Mazarico, F.G. Lemoine, G.A. Neumann, W. Kuang, T.J. Sabaka, et al. 2019. "Geodetic Evidence That Mercury Has A Solid Inner Core." *Geophysical Research Letters* 46 (7). https://doi.org/10.1029/2018GL081135.

[6] Konopliv, A. S., R. S. Park, and A. I. Ermakov. 2020. "The Mercury Gravity Field, Orientation, Love Number, and Ephemeris from the MESSENGER Radiometric Tracking Data." *Icarus* 335: 113386. https://doi.org/10.1016/J.ICARUS.2019.07.020.